Effect of different pseudopotentials on the phonon frequencies, dielectric constant, and Born effective charge of SnSe and SnSe$_2$ nanostructures: A density functional perturbation theory study

Elaheh Mohebbi [a], Eleonora Pavoni [a], Luca Pierantoni [b], Pierluigi Stipa [a], Emiliano Laudadio [a,*], Davide Mencarelli [b]

[a] *Department of Science and Engineering of Matter, Environment and Urban Planning (SIMAU), Marche Polytechnic University, 60131, Ancona, Italy*
[b] *Information Engineering Department, Marche Polytechnic University, 60131, Ancona, Italy*

A R T I C L E   I N F O

A B S T R A C T

The choice of the pseudopotentials (PPs) is a crucial step towards an accurate atomistic calculation of physical properties of 2D materials. In this study, based on Density-Functional Perturbation Theory (DFPT), we investigated the dependency of the phonon properties such as phonon frequencies, dielectric constant, Born effective charge, and vibrational modes of SnSe and SnSe$_2$ monolayers to the different types of PPs. On the basis of Generalized Gradient Approximation (GGA) using PBE functional, we computed eight phonon calculations for both lattices in combinations with four different PPs including Normconversing (NC) FHI/HGH, Ultrasoft (USPP), and Standard Solid-State (SSSP), while other parameters like cut-off energy, *k*-points mesh, and convergence threshold were kept fixed. However, the phonon properties of acoustic and optical phonons were better predicted by USPP and SSSP for phonon dispersion of SnSe and SnSe$_2$, respectively. Regarding the dielectric constant and Bohr effective charge calculations, our results showed that SnSe and SnSe$_2$ structures possess the dielectric tensor of 8.9 and 6.6 along the in-plane direction by using USPP calculations. Our outcomes also revealed less sensitivity of SnSe$_2$ polarization to the type of PPs by applying the electric field. This study recommends USPP and SSSP to further phonon analysis of other semiconductors.

1. Introduction

Two-dimensional (2D) van der Waals materials (vdWMs) such as graphene (Gr) [1], graphene-like materials [2], borophene [3], layered polymeric nitrogen (LP-N) [4], transition metal dichalcogenides (TMDCs) [5], group III$_A$–V$_A$ like 2D boron-carbon-nitride alloy [6], III$_A$–VI$_A$ structures such as GaSe [7], IV$_A$–VI$_A$ compounds [8], topological insulators [9], and perovskites [10], have significant interest thanks to their predominant photo-interaction [11], high carrier mobility [12], outstanding flexibility [13], direct-indirect band gap transitions [14], perfectly electrostatic controllability [15], and dangling-bond-free surface grown by vdW interactions [16].

Among them, graphene is a promising 2D material with band structure of Dirac cones and outstanding features for the design and implementation of a wide variety of devices, however, the low absorption efficiency of incident photons and the short lifetime of photoexcited carriers, resulted in an unsatisfactory in applications for electronics and optoelectronics devices. Then, some modifications in the graphene structure [2] could induced the semiconductor properties and optical band gap in the visible range of light, while an anomalously very low thermal conductivity of this nanosheet showed not promising property of that. Afterwards, layered molybdenum disulfide (MoS$_2$) with large direct band gaps is a possible choice to overcome the defects of graphene monolayer. However, the intrinsic bandgap of MoS$_2$ has the extremely low carrier mobility at room temperature [17] with the light response limited in the near infrared spectral region [18]. In our recent study of Mohebbi et al. [4], the LP-N structure has been investigated using density functional theory (DFT) calculations as a good substitution to BP, indicated desirable stability but very narrow band gap of 0.05 eV by calculating the band structure calculations.

Therefore, it is crucial to discover other 2D materials which owns a good geometrical and dynamical stability, appropriate electronic band gap, desirable carrier mobility, and remarkably high absorption coefficient to develop the high-performance devices. In this regard, 2D semiconducting materials, such as group IV$_A$ metal chalcogenides (metal = Ge, Sn, Pb; chalcogen = S, Se), have received great attention and extensive research interest because of their remarkably excellent electronic, photoelectronic, charge transport and thermal properties [19–21]. These materials can have the stoichiometric ratio and the formulation of MX (*e.g*, SnS, SnSe, SnTe) or MX$_2$ (*e.g.*, GeS$_2$, GeSe$_2$, SnS$_2$, SnSe$_2$) [22,23]. For instance, SnSe is a direct or indirect band gap (0.9–1.3 eV) semiconductor with a high absorption coefficient of 2×10^4 cm^{-1} and promising carrier mobility of 10^4 cm^2 V^{-1} s^{-1} [24]. On the other hand, SnSe$_2$ is an indirect band gap (1.0 eV) semiconductor with absorption coefficient of 1.3×10^4 cm^{-1} and carrier mobility lower than SnSe by 233 cm^2 V^{-1} s^{-1} [25,26]. It is worth noticing that different from TMDs, SnSe and SnSe$_2$ are rich in earth reserves and environmental-friendly elements with prominent chemical stability, making them particularly attractive for practical applications.

Despite recent advances in discovering different characteristics of SnSe and SnSe$_2$ materials, less properties related to their dynamic stability, phononic properties, polarization, and dielectric constant as well as their vibrational modes are present in the literatures, and the lattice dynamics of these 2D materials remain insufficiently understood. For this reason, implementing the theoretical approaches to study their excited carriers and transportation properties is of paramount importance. Onaiwu et al. [27], using DFT simulations and based on norm-conserving (NC) and ultra-soft Pseudopotentials (PPs) (USPP), estimated the phonon frequencies of graphene monolayer. They observed that the phonon dispersion strongly agrees with the experimental results by using the USPP. In another study by Jain et al. [28] have been employed three different PPs of USPP, NC and projector augmented-wave (PAW), to consider the phonon scattering processes and a full solution of the Boltzmann transport equation in crystalline silicon. The effects of exchange–correlation (XC) and PPs types on the DFT has driven good prediction of the thermal conductivity of 148 W/mK near to experimental value of 153 W/mK by applying the USPP and NC PPs. Further, in the research work by Wirtz et al. [29] DFT calculations with the generalized-gradient approximation (GGA) using Troullier –Martins (TM) PPs yields frequencies lower by 2 % than the local-density approximation (LDA) utilizing PAW PPs for the in-plane optical modes of phonon frequencies and is thus in more consistency with experiment evidence.

Here, we conducted comprehensive investigation into the lattice dynamics, phonon dispersion, Born effective charge, dielectric constant, and vibrational modes of SnSe and SnSe$_2$ monolayers based on ab-initio simulations of phonon calculations beyond perturbation theory. We performed eight calculations based on GGA/PBE xc functional with four different PPs of NC-FHI, NC-HGH, USPP, and recently released standard solid-state (SSSP), and an unprecedented number of computational resources for this type of analysis have been used. We discussed the need of testing several properties of these 2D materials showing how different PPs may yield similar results and convergence behaviors for one property but different ones for another property. Finally, we propose the best optimal PPs libraries chosen according to the testing protocol and criteria. This comprehensive computational study on 2D SnSe and SnSe$_2$ aims to shed light on the selection of the PPs for future purposes other relevant properties such as mobility, thermal conductivity, and group velocity of these two materials which are still under debating.

2. Computational methods

The lattice relaxation and total energy calculations of the SnSe and SnSe$_2$ nanosheets were investigated using Quantum espresso (QE) [30] and Quantum Atomistic ToolKit (ATK) [31] packages based on GGA adopting PBE functional [32]. An energy cutoff of 90 eV Ry was utilized for the plane-wave (PW) approach. Four different pseudopotentials consist of NC-FHI, NC-HGH [33], USPP [34] and SSSP [35] PPs were applied to treat valence electrons. The valence electron configuration considered in this calculation are 4d^{10}5s^2 5p^2 and 3d^{10}4s^2 4p^4 for Sn and Se respectively. Brillouin zone (BZ) was limited to the $12 \times 12 \times 1$ k-points for self-consistent field (SCF) calculations and a smearing value of 1×10^{-4} Ry was taken into account, while an $8 \times 8 \times 1$ and $12 \times 12 \times 1$ k-points mesh were used to predict the phonon modes of SnSe and SnSe$_2$ systems, respectively. Convergence criteria with respect to the total force and energy were chosen carefully to be 1×10^{-8} eV Å^{-1} and 1×10^{-5} eV, respectively.

To linear response to an electric field and to phonon calculations, considering a static perturbation $\partial V_0(r)$ to a system of electrons under an external potential $V_0(r)$ has been determined with [36–38],

$$\partial n(r) = \int \chi(r,\acute{r}) \partial V_0(r) d\acute{r} \tag{1}$$

where $n(r)$ is the electronic density distribution and $\chi(r,\acute{r})$ is the density response of the system.

The polarization charge $\partial n(r)$ produces an electrostatic field that screens the perturbing potential of $\partial V_0(r)$ with,

$$\partial V(r) = \partial V_0(r) + e^2 \int \frac{\partial n(r)}{|r - \acute{r}|} d\acute{r} \tag{2}$$

Then, we assume that the system obeys Kohn-Sham (KS) equations as,

$$(H_{KS} - \epsilon_i) = 0, \text{ and } H_{KS} = -\frac{\hbar^2}{2m}\nabla^2 + V_{KS}(r) \tag{3}$$

Where,

$$V_{KS}(r) = V_0(r) + V_H(r) + V_{xc}[n(r)] \tag{4}$$

While ϵ_i and $\hbar$ are eigenvalues and Planck's constant, and V_H and V_{xc} refer to Hartree–Fock and xc potentials.

And the charge is given by,

$$n(r) = \sum_i f_i |\psi_i(r)|^2 \tag{5}$$

Where f_i is non integer occupancy.

Then, an external $\partial V_0(r)$ has been added to $V_0(r)$, and then the first-order variation of KS become,

$$\partial \psi_i(r) = \sum_{j \neq i} \psi_j(r) \frac{\langle \psi_j | V_{KS} | \psi_i \rangle}{\epsilon_i - \epsilon_j} \tag{6}$$

And the perturbing potential represents a macroscopic electric field ∂E,

$$\partial V_0 = -e \partial E_0 \,.\, r \tag{7}$$

It is ill-defined in a crystal, because r is not a lattice-periodic operator, it can, however, be recast into a well-defined expression using the following trick,

$$[H_{KS}, r] = -\frac{\hbar^2}{m}\frac{\partial}{\partial r} + [V_{NL}, r] \tag{8}$$

Where V_{NL} is the nonlocal term of the potential.

Once $n(r)$ are calculated, the dynamical matrix can be easily derived, along with phonon modes and frequencies. To this end, we need to know the form of the second-order expansion term of the energy, which called *Density-Functional Perturbation Theory (DFPT)* [39].

We then assume that the external potential depends on some parameter λ.

$$\frac{\partial E}{\partial \lambda} = \int n(r) \frac{\partial V(r)}{\partial \lambda} dr \tag{9}$$

While first-order derivative $\partial E / \partial \lambda$ does not depend on any derivative

of $n(r)$ as Hellmann-Feynman theorem [40], and the second-order derivative $\partial^2 E/\partial^2 \lambda$ relevant on the first-order derivative of $\partial n(r)/\partial \lambda$ and the latter formula can be computed by SCF calculations in QE package.

In this regard, we need to remind that the behaviour of a system of interacting electrons r and nuclei R can be calculated by the solutions of the time-dependent Schrodinger equation [41] as,

$$i\hbar \frac{\partial \Phi(r,R;t)}{\partial t} = \left(-\sum_I \frac{\hbar^2}{2M_I} \frac{\partial^2}{\partial R_I^2} - \sum_i \frac{\hbar^2}{2m} \frac{\partial^2}{\partial r_i^2} \right) \Phi(r,R;t) \tag{10}$$

where $V(r,R)$ is the potential which describing the coulomb interactions by following Formula (11),

$$V(r,R) = \sum_{I>J} \frac{Z_I Z_J e^2}{|R_I - R_J|}$$
$$- \sum_{i,I} \frac{Z_I e^2}{|r_i - R_I|} + \sum_{i>j} \frac{e^2}{|r_i - r_j|} = V_{nn}(R) + V_{ne}(r,R) + V_{ee}(r) \tag{11}$$

Whereas Z is the charge and Born-Oppenheimer approximation valid for $M \gg m$.

The Born-Oppenheimer approximation allows to split the problem into an electronic (e) part depending upon nuclear (n) positions, and a nuclear part under an effective interatomic potential determined by the electrons. While the parameter $E(R)$ determines the *Potential Energy Surface* and the equilibrium geometry, the interatomic potential energy is expanded to 2nd order (harmonic approximation).

Normal mode frequencies ω and displacement patterns u_I^α for cartesian component α of atom I, at atomic position R_I, are determined by the secular equation [42] with,

$$\sum_{J,\beta} \left(C_{IJ}^{\alpha\beta} - M_I \omega^2 \delta_{IJ} \delta_{\alpha\beta} \right) U_J^\beta = 0 \tag{12}$$

where $C_{IJ}^{\alpha\beta}$ is the matrix of inter-atomic force constants (IFC), *i.e.*, second derivatives of the energy with respect to atomic position,

$$C_{IJ}^{\alpha\beta} \equiv \frac{\partial^2 E(\{R\})}{\partial R_I^\alpha \partial R_I^\beta} \tag{13}$$

We remind that in the crystals, normal modes are classified by a wave-vector q and the phonon frequencies $\omega(q)$ and displacement patterns $U_s^\alpha(q)$ are determined by,

$$\sum_{t,\beta} \left(\acute{C}_{st}^{\alpha\beta} - M_s \omega^2(q) \delta_{st} \delta_{\alpha\beta} \right) U_t^\beta(q) = 0 \tag{14}$$

This can be calculated from the knowledge of the linear response $\partial n(r)/\partial U_s^\alpha(q)$ and diagonalized to get phonon modes at q.

Fourier transform of force constants at q are second derivatives of the energy with respect to monochromatic perturbations,

$$\acute{C}_{st}^{\alpha\beta}(q) \equiv \sum_R e^{-iq.R} C_{st}^{\alpha\beta}(R) = \frac{1}{N_c} \frac{\partial^2 E}{\partial u_s^{*\alpha}(q) \partial u_t^{*\beta}(q)} \tag{15}$$

where $u_s^{*\alpha}$ denotes the displacement of atom s in the direction α. The second derivative of the energy in (15) is the change in the force acting on atom t in the direction β due to a displacement of the atom s in the direction α.

Coincidentally, the matrix of interatomic force constants is the sum of both the ionic and electronic contributions, *i.e.*,

$$\acute{C}_{st}^{\alpha\beta}(q) \equiv \acute{C}_{st}^{\alpha\beta}(q) \, (electron) + \acute{C}_{st}^{\alpha\beta}(q) \, (ion) \tag{16}$$

While,

$$V_{ion}(r) = \sum_{ls} v_s[r - R_l + \tau_s - u_s(l)] \tag{17}$$

Where R_l is the position of the l-th unit cell in the Bravais lattice, τ_s is the

equilibrium position of the unit cell, $u_s(l)$ is the deviation from equilibrium of the nuclear position and v_s is the ionic pseudopotential corresponding to the *s-th* atomic species.

3. Results and discussion

Based on GGA-PBE calculations using Quantum ATK code, the unit cells of SnSe (*Pnma*) and SnSe$_2$ (*P-3m1*) were simulated in Periodic Boundary Conditions (PBCs) along with three axes of Cartesian coordinate system. The optimized cells have been obtained with dimensions of a = 4.12625 Å, b = 4.70091 Å and c = 20 Å for SnSe and a = b = 3.8412 Å and c = 20 Å for SnSe$_2$ nanosheets, having orthorhombic and hexagonal lattices, respectively. The energy-lowest structures of the SnSe and SnSe$_2$ nanosheets are presented in Fig. 1 by the top and side views of both structures.

3.1. Phonons band structures

The analysis of phonon band structure can provide a reliable test for the dynamical stability of the structures. We calculated the phonon dispersion curves along with the directions of G–M– K– G in the first BZ in the reciprocal space using different PPs of NC-FHI, NC-HGH, USPP, and SSSP (as you see in Figs. 2 and 3). According to different lattices, we have twelve and nine phonon modes for SnSe and SnSe$_2$ structures since there are 3 atoms (1 Sn and 2 Se) and 4 atoms (2 Sn and 2 Se) inside their unit cells, respectively.

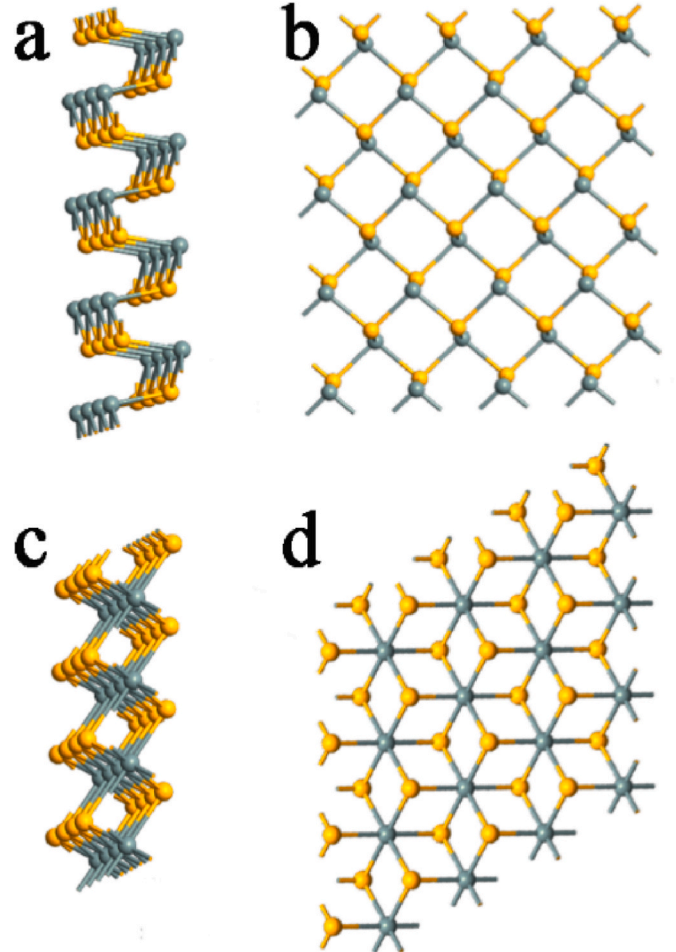The maximum frequency calculated for SnSe monolayer can be

Fig. 1. Top and side views of the optimized configurations for SnSe (a, b) and SnSe$_2$ (c, d) monolayers; the grey and gold sticks are the Sn and Se atoms.
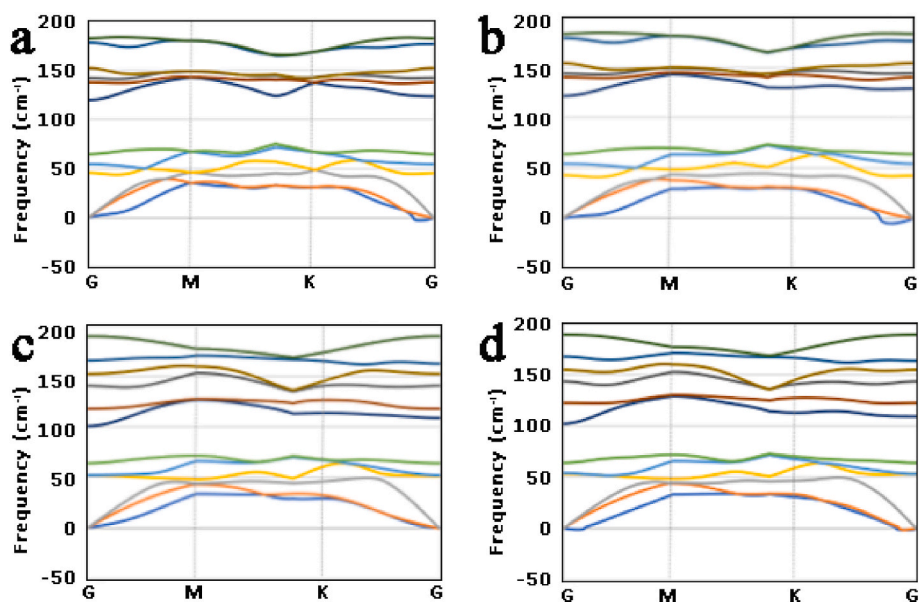
Fig. 2. Phonon band structure of SnSe nanosheet using NC-FHI (a), NC-HGH (b), USPP (c), SSSP (d).
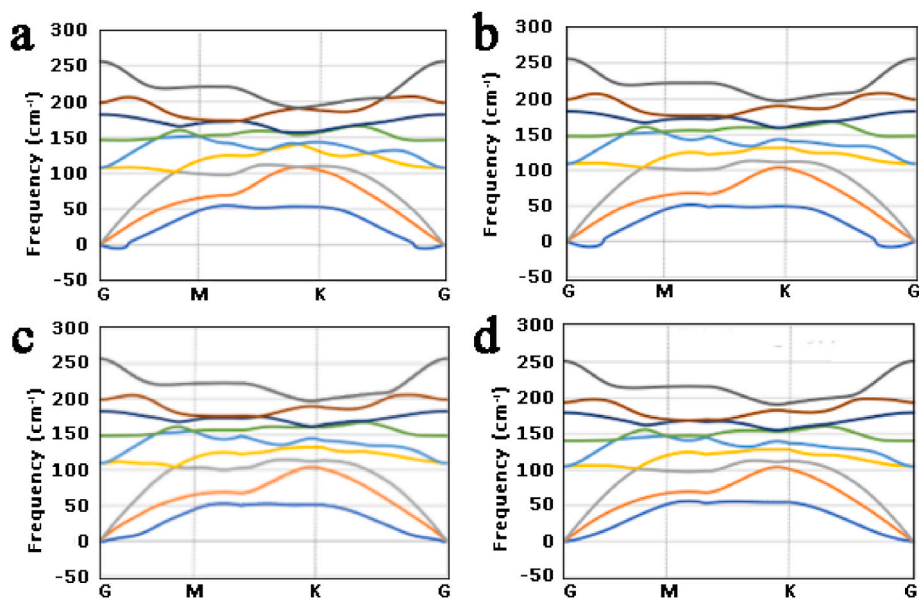

Fig. 3. Phonon band structure of SnSe$_2$ nanosheet using NC-FHI (a), NC-HGH (b), USPP (c), SSSP (d).

found near to 200 cm^{-1} while SnSe$_2$ showing higher frequencies at 300 cm^{-1}. For both systems, the most noteworthy point is that the two acoustic modes present linear dispersion, whereas the remaining one shows a quadratic dispersion, as the signatures of 2D nanomaterials. By comparison of phonon band structure of SnSe and SnSe$_2$, there exists an evident phonon gap (about 40–60 cm^{-1}) between the irreducible representations of phonon modes for SnSe owing to its larger cation/anion mass ratio, whereas there is no gap of phonon bands for SnSe$_2$ structure. As shown in Fig. 2 for SnSe nanosheet, while NC-FHI, NC-HGH, and SSSP PPs indicated the negative frequencies for acoustic modes near to the gamma point in first BZ, USPP has resulted in the phonon dispersion with no imaginary frequency in the mesh points in the reciprocal space, which reveal that the kinetical stability of this monolayer.

In detail, inspection of Fig. 2 implies that for the acoustic vibration frequencies of monolayer SnSe, negative frequencies can be seen along K-G bands in reciprocal space with using NC-FHI and NC-HGH PPs, whereas using SSSP show non real frequencies along G-K and M-G in the

first BZ in the lattice. On the other hand, the position of optical frequencies between 100 and 200 cm^{-1} can significantly alter by changing the type of PPs. As observe in Fig. 2, the vibrational frequencies had downward shift to the lower frequencies by using the USPP and SSSP PPs around 100 cm^{-1}, while corresponded curves indicate higher frequency values, around 125 cm^{-1}, about the less-accurate NC-FHI and NC-HGH approximations. Clearly, as seen in Fig. 2, while applying different PPs of NC-FHI, NC-HGH, and USPP were not able to change the phonon modes position for SnSe$_2$, SSSP resulted in downshift of optical frequencies with a difference of 6 cm^{-1}. Importantly, the present of imaginary frequencies close to the gamma point can significantly influence by the type of PPs. The phonon frequencies in Fig. 3 related to SnSe$_2$ monolayer indicated that SSSP PPs can provide all vibration real modes of acoustic modes in the entire BZ, while other three PPs showed negative frequencies near to the center of reciprocal space. The number of negative frequencies calculated by NC-HGH are remarkably more than those computed by NC-FHI, and USPP predicted the phonon

dispersion curve similar to SSSP with only low number of not real frequencies. The IR and Raman frequencies of SnSe and SnSe$_2$ monolayer have been calculated at G point in the first BZ, and they are available in Table S1 in Supplementary Material file.

In order to compare the phonon frequencies in the center of BZ, we reported all the frequencies of phonon modes at gamma point for both SnSe and SnSe$_2$ materials calculated by more accurate SSSP and USPP PPs at cm^{-1} and THz units (Table 1). These outcomes reveal how using different PPs can change near-zero acoustic frequencies for two structures with the same elements. About the SnSe, the frequencies are changed from -3.57 cm^{-1} (-0.107 THz) and -1.66 cm^{-1}(-0.049 THz) using SSSP to 6.65 cm^{-1} (0.199 THz) and 6.83 cm^{-1} (0.204 THz) in USPP, respectively. These frequency differences are slightly decreased for SnSe$_2$ with -2.35 cm^{-1} (-0.070 THz) and -2.11 cm^{-1} (-0.063 THz) using USPP to 1.38 cm^{-1} (0.041 THz) and 1.44 cm^{-1} (0.043 THz) by SSSP, respectively.

3.2. Dielectric tensor and Born effective charges

According to LO–TO splitting in the materials in the present of electric field, macroscopic electric field incompatible with PBCs and must be separately treated. Phenomenological expression for the energy (**E**) as a function of atomic displacements and of macroscopic electric field (*E*) will be [36–38],

Table 1
Phonon frequencies of SnSe and SnSe$_2$ lattices at gamma point in the first BZ calculated by USPP (X(Sn,Se).pbe-dnrrkjus_psl.1.0.0.UPF) and SSSP (X(Sn,Se) _pbe_v1.uspp.F.UPF).

	USPP	SSSP
SnSe	freq (1) = 0.199534 [THz] = 6.655753 [cm^{-1}]	freq (1) = −0.107032 [THz] = −3.570210 [cm^{-1}]
	freq (2) = 0.204774 [THz] = 6.830539 [cm^{-1}]	freq (2) = −0.049974 [THz] = −1.666951 [cm^{-1}]
	freq (3) = 0.224892 [THz] = 7.501602 [cm^{-1}]	freq (3) = 0.036697 [THz] = 1.224076 [cm^{-1}]
	freq (4) = 1.540028 [THz] = 51.369805 [cm^{-1}]	freq (4) = 1.577889 [THz] = 52.632697 [cm^{-1}]
	freq (5) = 1.587825 [THz] = 52.964150 [cm^{-1}]	freq (5) = 1.597634 [THz] = 53.291325 [cm^{-1}]
	freq (6) = 1.922631 [THz] = 64.132052 [cm^{-1}]	freq (6) = 1.924688 [THz] = 64.200689 [cm^{-1}]
	freq (7) = 3.045018 [THz] = 101.570870 [cm^{-1}]	freq (7) = 3.070202 [THz] = 102.410919 [cm^{-1}]
	freq (8) = 3.546809 [THz] = 118.308804 [cm^{-1}]	freq (8) = 3.613386 [THz] = 120.529599 [cm^{-1}]
	freq (9) = 3.653430 [THz] = 121.865309 [cm^{-1}]	freq (9) = 3.671979 [THz] = 122.484051 [cm^{-1}]
	freq (10) = 4.239545 [THz] = 141.416015 [cm^{-1}]	freq (10) = 4.305026 [THz] = 143.600201 [cm^{-1}]
	freq (11) = 4.615876 [THz] = 153.969063 [cm^{-1}]	freq (11) = 4.668931 [THz] = 155.738765 [cm^{-1}]
	freq (12) = 5.695908 [THz] = 189.995050 [cm^{-1}]	freq (12) = 5.665477 [THz] = 188.979987 [cm^{-1}]
SnSe$_2$	freq (1) = −0.070592 [THz] = −2.354698 [cm^{-1}]	freq (1) = 0.041597 [THz] = 1.387523 [cm^{-1}]
	freq (2) = −0.063315 [THz] = −2.111955 [cm^{-1}]	freq (2) = 0.043349 [THz] = 1.445952 [cm^{-1}]
	freq (3) = −0.063315 [THz] = −2.111955 [cm^{-1}]	freq (3) = 0.043349 [THz] = 1.445952 [cm^{-1}]
	freq (4) = 3.107453 [THz] = 103.653478 [cm^{-1}]	freq (4) = 3.139876 [THz] = 104.734995 [cm^{-1}]
	freq (5) = 3.107453 [THz] = 103.653478 [cm^{-1}]	freq (5) = 3.139876 [THz] = 104.734995 [cm^{-1}]
	freq (6) = 4.143660 [THz] = 138.217616 [cm^{-1}]	freq (6) = 4.201800 [THz] = 140.156948 [cm^{-1}]
	freq (7) = 4.143660 [THz] = 138.217616 [cm^{-1}]	freq (7) = 4.201800 [THz] = 140.156948 [cm^{-1}]
	freq (8) = 5.341386 [THz] = 178.169451 [cm^{-1}]	freq (8) = 5.370969 [THz] = 179.156227 [cm^{-1}]
	freq (9) = 7.515552 [THz] = 250.691827 [cm^{-1}]	freq (9) = 7.511617 [THz] = 250.560575 [cm^{-1}]

$$(\{U\}, E) \equiv \frac{1}{2} \sum_{st} \sum_{\alpha\beta} u_s \, . \acute{C}_{st} . u_t - \frac{\Omega}{8\pi} E \, . \, \epsilon_\infty . \, E - e \sum_s u_s \, . \, Z_s^* . \, E \tag{18}$$

Where $\acute{C}_{st}$, ϵ_∞, and Z_s^* refer to force constants, dielectric tensor, and Born effective charge, respectively.

To solve the linear response to a macroscopic electric field, we need to iterate over $V_{SCF}(r)$ while keeping E fixed,

$$\frac{\partial V_{SCF}(r)}{\partial E} = \frac{\partial V(r)}{\partial E} + \int \left(\frac{e^2}{|r - r|} + \frac{\partial v_{xc}(r)}{\partial n(\acute{r})} \right) + \frac{\partial n(\acute{r})}{\partial E} d\acute{r} \tag{19}$$

Dielectric tensor ϵ_∞^{ab} are related to polarization induced by an electric field E which can determined by,

$$\epsilon_\infty^{ab} = \delta_{ab} + 4\pi \frac{\partial p_a}{\partial E_\beta}|u_{s\,(q=0)=0} \tag{20}$$

And,

$$\epsilon_\infty^{ab} = \delta_{\alpha\beta} - \frac{1}{N_c} \frac{\partial^2 E}{\partial E_\alpha \partial E_\beta} \tag{21}$$

Where δ and N_c are electronic screening and the number of the cells in the crystal.

Finally, we have

$$\epsilon_\infty^{ab} = \delta_{\alpha\beta} + \frac{16\pi e}{N_c \Omega} \sum_{n=1}^{N/2} \langle \psi_n^\alpha | \frac{\partial \psi_n}{\partial E_\beta} \rangle \tag{22}$$

And we need to properly deal with LO-TO splitting in phonons which are three additional linear-response calculations to an electric field.

Our calculated dielectric constants of SnSe and SnSe$_2$ structures are illustrated in Fig. 4. It is worth noticing that the ionic contribution to the dielectric constant of SnSe and SnSe$_2$ along the out-of-plane (c axis) direction is lower with respect to in-plane (a and b axis) directions, which reveal the 2D characteristics of both materials. The evaluation of the dielectric constants obtained from DFT-based electric field calculations of monolayers SnSe and SnSe$_2$ indicate that the dielectric tensor can significantly vary with the change in the PPs type. As you see in Fig. 4, the maximum dielectric constant related to SnSe nanosheet found to be 8.9 which has been computed by USPP and the corresponding value for SnSe$_2$ monolayer is 6.66 (a bit lower) has been obtained from NC-HGH and USPP, respectively. Our outcome obtained from GGA-PBE show excellent consistency with the previous experimental studies reported in Refs. [43,44] with the dielectric constant of 9.0 and 7.4 for SnSe and SnSe$_2$, while the those computed with DFT calculations have been reported substantially lower values of 5.4 [45] and 4.1 [46], respectively.

The effective charge tensor quantifies the electric response of a crystal to internal displacements of its atoms. Effective charges Z^* are related to polarization p induced by a lattice distortion can defined through,

$$Z_s^{*\alpha\beta} = \frac{\Omega}{e} \frac{\partial p_\alpha}{\partial u_s^\beta (q=0)} \tag{23}$$

One can observe that such quantities are second derivatives of the energy as well,

$$Z_s^{*\alpha\beta} = Z_s \delta_{\alpha\beta} - \frac{1}{N_c} \frac{\partial^2 E}{\partial E_\alpha \partial u_s^\beta (q=0)} \tag{24}$$

And polarization induced by an atomic displacement can be calculated by,

$$\frac{\partial p_\alpha}{\partial u_s^\beta (q=0)} = \frac{\Omega}{N_c e} \int \frac{\partial n(r)}{\partial u_s (q=0)} dr + \frac{e}{\Omega} Z_s \, \delta_{\alpha\beta} \tag{25}$$
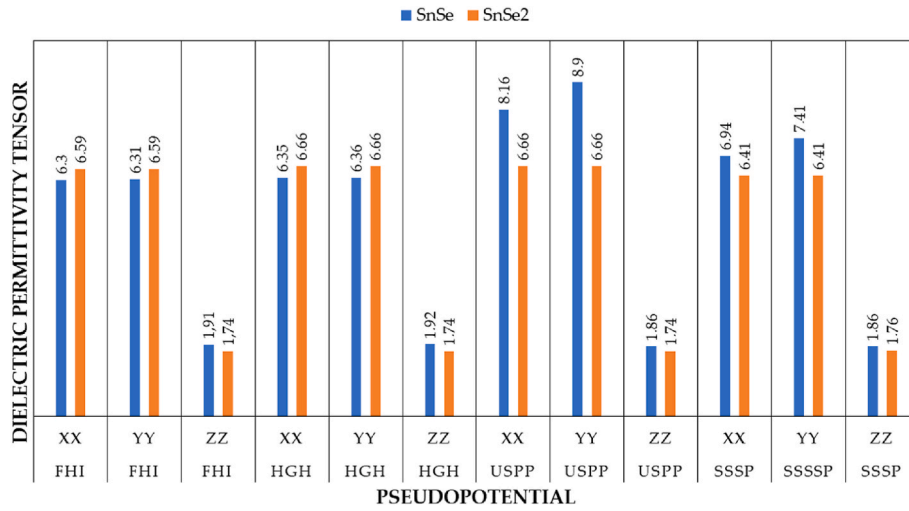
Fig. 4. Dielectric constant obtained from electric fields calculation for SnSe and SnSe$_2$ nanostructures using different PPs of NC-FHI, NC-HGH, USPP, and SSSP.

While effective charges are then given by,

$$Z_s^{*\alpha\beta} = Z_s + \frac{4}{N_c} \sum_{n=1}^{N/2} \langle \psi_n^\alpha \left| \frac{\partial \psi_n}{\partial u_\beta(q=0)} \right\rangle \tag{26}$$

Using the linear response to an atomic perturbation.

Alternatively, effective charges obtained by the force linearly induced on an atom by an electric field formulated by,

$$Z_s^{*\alpha\beta} = Z_s + \frac{4}{N_c} \sum_{n=1}^{N/2} \langle \psi_n \left| \frac{\partial V}{\partial u_\beta(q=0)} \right| \frac{\partial \psi_n}{\partial E_\alpha} \rangle \tag{27}$$

The Born effective charges Z* (Sn) and Z* (Se) along cartesian axis are calculated for SnSe and SnSe$_2$ monolayers, as seen in Tables S2 and S3 (Supplementary Material). Inspection in both tables reveal that very good agreement results with dielectric tensor calculations in Fig. 4, by applying different PPs of NC-FHI, NC-HGH, USPP, and SSSP. While for SnSe lattice an increase of the Z* (Sn) and Z* (Se) amounts can be observed yielded by USPP (which results from the higher LO-TO splitting and the high-frequency dielectric constant), polarization of elements in SnSe$_2$ lattice turn out to be nearly constant for NC-FHI, NC-HGH and USPP and a bit smaller with SSSP. In consistency to dielectric tensor values of SnSe$_2$ in Fig. 4, using SSSP resulted in lower dielectric constant of 6.41 along the in-plane direction comparable with amounts of 6.59 (NC–FHI) and 6.66 (NC-HGH and USPP) in the same axis direction. These predicted values indicate that the Born effective charge and dielectric tensor of SnSe is found to be more sensitive to the type of PPs where more accurate USPP and SSSP have given higher dielectric constant for this 2D material, whereas the polarization of SnSe$_2$ in the present of electric field did not show remarkable dependency to the variation of PPs.

3.3. Phonon density of states and vibrational modes

The phonon density of states (DOS) of SnSe and SnSe$_2$ monolayers at 300 K are shown in Fig. 5 and have been calculated by USPP and SSSP for SnSe and SnSe$_2$, respectively. We focus on these two PPs since they resulted in more accurate phonon band structure and dielectric tensor as well as Born effective charges. For this simulation, we have the normal modes, Raman and Infrared (IR) intensities. Calculation of IR scattering peaks can be followed by Refs. [36–38],

$$I_{IR(\nu)} = \sum_\alpha \left| \sum_{s\beta} Z_s^{*\alpha\beta} U_s^\beta(\nu) \right|^2 \tag{28}$$

And Raman coefficients are third-order derivatives of the energy that can be calculated directly from effective charges and phonon displacement patterns.

The non-resonant Raman intensities can be formulated as,

$$I(\nu) \propto \frac{(\omega_i - \omega_\nu)^4}{\omega_\nu} r_{\alpha\beta}(\nu), \quad r_{\alpha\beta}(\nu) = \left| \frac{\partial \chi_{\alpha\beta}}{\partial U(\nu)} \right|^2 \tag{29}$$

where χ is the electric polarizability of the system.

2D SnSe monolayer have 12 irreducible representations of phonon modes and, as see in Fig. 5, four Raman A_g modes have the frequency position of $A_g^1 = 32$ cm^{-1}, $A_g^2 = 67$ cm^{-1}, $A_g^3 = 126$ cm^{-1}, and $A_g^4 = 154$ cm^{-1}, whereas the Raman mode of B_{3g}^1 and B_{3g}^2 have frequencies of 34 cm^{-1} and 116 cm^{-1}, respectively. Our results for SnSe show similarity to the experimental measurements of Sriv et al. [47] with corresponding Raman modes of A_g^1, B_{3g}^1, A_g^2, A_g^3, B_{3g}^2 and A_g^4 at frequencies of 32 cm^{-1},
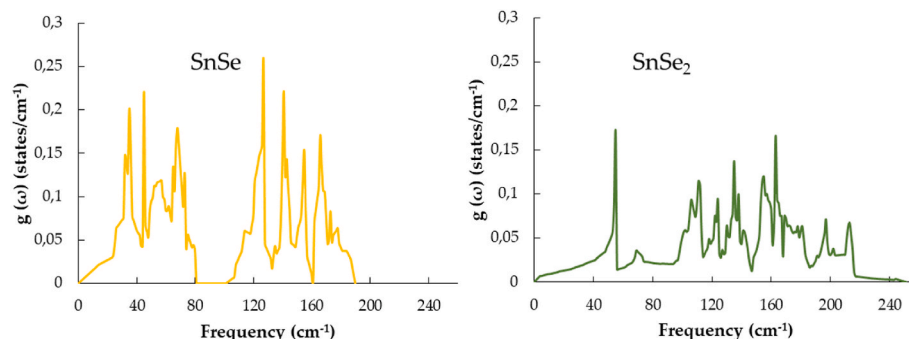

Fig. 5. Phonon Density of States(g(ω)) SnSe and SnSe$_2$ structures including normal modes, Raman and IR intensities.

37 cm^{-1}, 70 cm^{-1}, 109 cm^{-1}, 131 cm^{-1}, and 150 cm^{-1} for a 632 nm-thickness SnSe.

Instead, the six irreducible representations of phonon modes for SnSe$_2$ can presented as $A_g^1 + 2A_{2u} + E_g + 2E_u$. while the acoustic modes are $A_{2u} + E_u$, and there are four optical modes of $A_g^1 + E_g$ related to Raman intensities and two $A_u + E_u$ attributed to IR modes. In this study the calculated frequencies of A_g^1 and E_g are 196 cm^{-1} and 111 cm^{-1}, respectively, while the IR modes are $A_{2u}^1 = 246$ cm^{-1}, $A_{2u}^2 = 212$ cm^{-1}, $E_u^1 = 207$ cm^{-1}, $E_u^2 = 141$ cm^{-1}. The computed values for vibrational Raman frequencies of SnSe$_2$ monolayer in this study are in good consistency with the experimental evidence of $A_g = 186$ cm^{-1} and $E_g = 111$ cm^{-1} for a SnSe$_2$ thin film [48].

4. Conclusions

In this work, the dependence of the various properties of the phonon dispersion and softening, dielectric tensor and the Born effective charge of SnSe and SnSe$_2$ monolayers on the particular PPs of NC-FHI, NC-HGH, USPP, and SSSP had been investigated using first-principles DFPT calculations. Interatomic force constants and the phonon-band structure are then obtained by computing the Fourier transform of dynamical matrices on a regular mesh of wave vectors. We demonstrated that the various acoustic and optical branches of the phonon frequencies at the special k-points depend greatly on the type of PPs. While both 2D materials shown two linear and one quadratic dispersions in their acoustic modes, phonon calculations based on USPP and SSSP resulted the high-precision phonon band structure with all real frequencies near to gamma points in the center of BZ, for SnSe and SnSe$_2$ nanosheets, respectively. Then, the dielectric tensor and Born effective charges are determined by applying the electric field for SnSe and SnSe$_2$ on their orthorhombic and hexagonal lattices. The outcomes showed that SnSe and SnSe$_2$ with dielectric tensor of 8.9 and 6.6 calculated by USPP are in very good consistency with the available experimental observations. In the good agreement with dielectric constant calculations, the estimated Born effective charge implied dependency of SnSe nanostructure to the choice of PPs with higher amounts of Z*(Sn) and Z*(Se) by USPP, while those corresponded to SnSe$_2$ revealed that a different behavior with less sensitivity to the type of PPs. The calculated phonon density of states yielded good consistency with the experimental Raman frequencies in both nanostructures.

Altogether, the main aim of this computational study is to provide an overview of phonon modes and frequencies and dielectric constant as well as lattice polarization of SnSe and SnSe$_2$ materials for considering their transportation properties in the future work and some promising applications in THz adsorption technology.

Author Contributions

Author Contributions: Conceptualization, E.M., E.L. and P.S.; methodology, E.M. and E.L.; validation, E.M., E.L., P.S., L.P., and D.M; investigation, E.M.; data curation, E.M.; writing—original draft preparation, E.M.; writing—review and editing, E.M., E.L., E.P., P.S., L.P., and D.M.; visualization, E.M.; supervision, P.S.; project administration, E.M., E.L., E.P., P.S., L.P. and D.M. All authors have read and agreed to the published version of the manuscript.

Declaration of competing interest

The authors declare the following financial interests/personal relationships which may be considered as potential competing interests: Laudadio Emiliano reports financial support was provided by Polytechnic University of Marche.

Data availability

No data was used for the research described in the article.

Appendix A. Supplementary data

Supplementary data to this article can be found online at https://doi.org/10.1016/j.jpcs.2023.111755.

References

[1] C.-H. Liu, Y.-C. Chang, T.B. Norris, Z. Zhong, Graphene photodetectors with ultra-broadband and high responsivity at room temperature, Nat. Nanotechnol. 9 (2014) 273–278.

[2] E. Mohebbi, M.M.S. Fakhrabadi, Electronic, optical, mechanical, and thermal properties of diphenylacetylene-based graphyne nanosheet using density functional theory, Nanotechnology 32 (2021), 405705.

[3] A.J. Mannix, X.-F. Zhou, B. Kiraly, J.D. Wood, D. Alducin, B.D. Myers, X. Liu, B.L. Fisher, U. Santiago, J.R. Guest, Synthesis of borophenes: anisotropic, two-dimensional boron polymorphs, Science 350 (2015) (1979) 1513–1516.

[4] E. Mohebbi, M.M.S. Fakhrabadi, First-principles calculations to investigate strain-tunable electronic bandgap of black phosphorus-structured nitrogen with desirable optical and elastic properties, Mater. Sci. Eng. B 281 (2022), 115745.

[5] A.M. Jones, H. Yu, N.J. Ghimire, S. Wu, G. Aivazian, J.S. Ross, B. Zhao, J. Yan, D.G. Mandrus, D. Xiao, Optical generation of excitonic valley coherence in monolayer WSe2, Nat. Nanotechnol. 8 (2013) 634–638.

[6] J. Lu, K. Zhang, X. Feng Liu, H. Zhang, T. Chien Sum, A.H. Castro Neto, K.P. Loh, Order–disorder transition in a two-dimensional boron–carbon–nitride alloy, Nat. Commun. 4 (2013) 2681.

[7] X. Xiong, Q. Zhang, X. Zhou, B. Jin, H. Li, T. Zhai, One-step synthesis of p-type GaSe nanoribbons and their excellent performance in photodetectors and phototransistors, J. Mater. Chem. C Mater. 4 (2016) 7817–7823.

[8] D. Yang, B. Li, C. Hu, H. Deng, D. Dong, X. Yang, K. Qiao, S. Yuan, H. Song, Controllable growth orientation of SnS2 flakes for low-noise, high-photoswitching ratio, and ultrafast phototransistors, Adv. Opt. Mater. 4 (2016) 419–426.

[9] J. Besbas, K. Banerjee, J. Son, Y. Wang, Y. Wu, M. Brahlek, N. Koirala, J. Moon, S. Oh, H. Yang, Helicity-dependent photovoltaic effect in Bi2Se3 under normal incident light, Adv. Opt. Mater. 4 (2016) 1642–1650.

[10] J. Song, L. Xu, J. Li, J. Xue, Y. Dong, X. Li, H. Zeng, Monolayer and few-layer all-inorganic perovskites as a new family of two-dimensional semiconductors for printable optoelectronic devices, Adv. Mater. 28 (2016) 4861–4869.

[11] L. Britnell, R.M. Ribeiro, A. Eckmann, R. Jalil, B.D. Belle, A. Mishchenko, Y.-J. Kim, R.V Gorbachev, T. Georgiou, S. V Morozov, Strong light-matter interactions in heterostructures of atomically thin films, Science 340 (2013) (1979) 1311–1314.

[12] S. Kim, A. Konar, W.-S. Hwang, J.H. Lee, J. Lee, J. Yang, C. Jung, H. Kim, J.-B. Yoo, J.-Y. Choi, High-mobility and low-power thin-film transistors based on multilayer MoS2 crystals, Nat. Commun. 3 (2012) 1011.

[13] H. Peng, W. Dang, J. Cao, Y. Chen, D. Wu, W. Zheng, H. Li, Z.-X. Shen, Z. Liu, Topological insulator nanostructures for near-infrared transparent flexible electrodes, Nat. Chem. 4 (2012) 281–286.

[14] S. Zhang, Z. Yan, Y. Li, Z. Chen, H. Zeng, Atomically thin arsenene and antimonene: semimetal–semiconductor and indirect–direct band-gap transitions, Angew. Chem. Int. Ed. 54 (2015) 3112–3115.

[15] W. Feng, X. Zhou, W.Q. Tian, W. Zheng, P. Hu, Performance improvement of multilayer InSe transistors with optimized metal contacts, Phys. Chem. Chem. Phys. 17 (2015) 3653–3658.

[16] J. Ji, X. Song, J. Liu, Z. Yan, C. Huo, S. Zhang, M. Su, L. Liao, W. Wang, Z. Ni, Two-dimensional antimonene single crystals grown by van der Waals epitaxy, Nat. Commun. 7 (2016) 13352.

[17] S.H. Mir, V.K. Yadav, J.K. Singh, Recent advances in the carrier mobility of two-dimensional materials: a theoretical perspective, ACS Omega 5 (2020) 14203–14211.

[18] Y. Xie, B. Zhang, S. Wang, D. Wang, A. Wang, Z. Wang, H. Yu, H. Zhang, Y. Chen, M. Zhao, Ultrabroadband MoS2 photodetector with spectral response from 445 to 2717 nm, Adv. Mater. 29 (2017), 1605972.

[19] S. Kumar, Z.H. Khan, M.A.M. Khan, M. Husain, Studies on thin films of lead chalcogenides, Curr. Appl. Phys. 5 (2005) 561–566.

[20] X. Zhou, X. Hu, S. Zhou, Q. Zhang, H. Li, T. Zhai, Ultrathin 2D GeSe2 rhombic flakes with high anisotropy realized by van der Waals epitaxy, Adv. Funct. Mater. 27 (2017), 1703858.

[21] P. Yu, X. Yu, W. Lu, H. Lin, L. Sun, K. Du, F. Liu, W. Fu, Q. Zeng, Z. Shen, Fast photoresponse from 1T tin diselenide atomic layers, Adv. Funct. Mater. 26 (2016) 137–145.

[22] J. Yao, G. Yang, 2D material broadband photodetectors, Nanoscale 12 (2020) 454–476.

[23] D. Lu, C. Yue, S. Luo, Z. Li, W. Xue, X. Qi, J. Zhong, Phase controllable synthesis of SnSe and SnSe2 films with tunable photoresponse properties, Appl. Surf. Sci. 541 (2021), 148615.

[24] B. Wang, S.P. Zhong, Z. Bin Zhang, Z.Q. Zheng, Y.P. Zhang, H. Zhang, Broadband photodetectors based on 2D group IVA metal chalcogenides semiconductors, Appl. Mater. Today 15 (2019) 115–138.

[25] C. Guo, Z. Tian, Y. Xiao, Q. Mi, J. Xue, Field-effect transistors of high-mobility few-layer SnSe2, Appl. Phys. Lett. 109 (2016).

[26] C. Cheng, Z. Li, N. Dong, J. Wang, F. Chen, Tin diselenide as a new saturable absorber for generation of laser pulses at 1μm, Opt Express 25 (2017) 6132–6140.

[27] K.N. Onaiwu, J.O.A. Idiodi, Effects of pseudopotentials on the phonon dispersion of graphene, IOSR J. Appl. Phys. 6 (2014) 27–33.

[28] A. Jain, A.J.H. McGaughey, Effect of exchange–correlation on first-principles-driven lattice thermal conductivity predictions of crystalline silicon, Comput. Mater. Sci. 110 (2015) 115–120.

[29] L. Wirtz, A. Rubio, The phonon dispersion of graphite revisited, Solid State Commun. 131 (2004) 141–152.

[30] P. Giannozzi, S. Baroni, N. Bonini, M. Calandra, R. Car, C. Cavazzoni, D. Ceresoli, G.L. Chiarotti, M. Cococcioni, I. Dabo, Quantum espresso: a modular and open-source software project for quantum simulations of materials, J. Phys. Condens. Matter 21 (2009), 395502.

[31] S. Smidstrup, T. Markussen, P. Vancraeyveld, J. Wellendorff, J. Schneider, T. Gunst, B. Verstichel, D. Stradi, P.A. Khomyakov, U.G. Vej-Hansen, QuantumATK: an integrated platform of electronic and atomic-scale modelling tools, J. Phys. Condens. Matter 32 (2019), 015901.

[32] Z. Wu, R.E. Cohen, More accurate generalized gradient approximation for solids, Phys. Rev. B 73 (2006), 235116.

[33] D.R. Hamann, Optimized norm-conserving Vanderbilt pseudopotentials, Phys. Rev. B 88 (2013), 085117.

[34] X. Qian, J. Li, X. Lin, S. Yip, Time-dependent density functional theory with ultrasoft pseudopotentials: real-time electron propagation across a molecular junction, Phys. Rev. B 73 (2006), 035408.

[35] G. Prandini, A. Marrazzo, I.E. Castelli, N. Mounet, N. Marzari, Precision and efficiency in solid-state pseudopotential calculations, npj Comput. Mater. 4 (2018) 72.

[36] S. Baroni, S. De Gironcoli, A. Dal Corso, P. Giannozzi, Phonons and related crystal properties from density-functional perturbation theory, Rev. Mod. Phys. 73 (2001) 515.

[37] P. Vogl, Microscopic theory of electron-phonon interaction in insulators or semiconductors, Phys. Rev. B 13 (1976) 694.

[38] L. Wendler, R. Haupt, Electron–phonon interaction in semi-infinite semiconductor superlattices, Phys. Status Solidi 141 (1987) 493–505.

[39] S. Wei, M.Y. Chou, Ab initio calculation of force constants and full phonon dispersions, Phys. Rev. Lett. 69 (1992) 2799.

[40] P. Politzer, J.S. Murray, The Hellmann-Feynman theorem: a perspective, J. Mol. Model. 24 (2018) 1–7.

[41] H. Tal-Ezer, R. Kosloff, An accurate and efficient scheme for propagating the time dependent Schrödinger equation, J. Chem. Phys. 81 (1984) 3967–3971.

[42] J. Szeftel, A. Khater, Calculation of surface phonons and resonances: the matching procedure revisited: I, J. Phys. C Solid State Phys. 20 (1987) 4725.

[43] K.S. Urmila, T.A. Namitha, J. Rajani, R.R. Philip, B. Pradeep, Optoelectronic properties and Seebeck coefficient in SnSe thin films, J. Semiconduct. 37 (2016), 093002.

[44] Y. Huang, X. Chen, D. Zhou, H. Liu, C. Wang, J. Du, L. Ning, S. Wang, Stabilities, electronic and optical properties of SnSe2 (1−x) S2 x alloys: a first-principles study, J. Phys. Chem. C 120 (2016) 5839–5847.

[45] Z. Cui, X. Wang, Y. Ding, M. Li, Exploration work function and optical properties of monolayer SnSe allotropes, Superlattice. Microst. 114 (2018) 251–258.

[46] M.M. El-Nahass, Optical properties of tin diselenide films, J. Mater. Sci. 27 (1992) 6597–6604.

[47] T. Sriv, T.M.H. Nguyen, Y. Lee, S.Y. Lim, V.Q. Nguyen, K. Kim, S. Cho, H. Cheong, Optical phonons of SnSe (1−x) S x layered semiconductor alloys, Sci. Rep. 10 (2020), 11761.

[48] M. Kang, S. Rathi, I. Lee, L. Li, M.A. Khan, D. Lim, Y. Lee, J. Park, A.T. Pham, A.T. Duong, Photodetector based on multilayer SnSe2 field effect transistor, J. Nanosci. Nanotechnol. 18 (2018) 4243–4247.